BNL-229327-2026-JAAM

In-situ monitoring of atomically dispersed Pt sites supported on OMS-2 during CO2 activation

S. Bamonte, A. I. Frenkel

To be published in "Applied Catalysis B: Environment and Energy"

November 2025

Chemistry Department

Brookhaven National Laboratory

U.S. Department of Energy

USDOE Office of Science (SC), Basic Energy Sciences (BES). Chemical Sciences, Geosciences & Biosciences Division (CSGB)

DISCLAIMER

In-situ Monitoring of Atomically Dispersed Pt sites supported on OMS-2 during CO_2 activation

Scott Bamonte[1], Harshul S. Khanna[1],Inosh Perera[2], Meilin Li[2], Luisa F Posada[2], Seth March[2], Nicholas A. Eddy[1], Ryuichi Shimogawa[3,4],Amelia Figueroa[5], Chao Li[2], Seth Shuster[2], Haiyan Tan[6], Nebojsa Marinkovic[7], Ashley R. Head[8], Dmitri N. Zakharov[8], Lu Ma[9], Pu-Xian Gao[1], Anatoly I. Frenkel,[3,10] Steven L. Suib[1,2]

1. Institute of Materials Sciences, University of Connecticut, 25 King Hill Rd., Storrs, CT 06269, United States

2. Department of Chemistry, University of Connecticut, 55 N. Eagleville Rd., Storrs, CT 06269, United States

3. Department of Materials Science and Chemical Engineering, Stony Brook University, Stony Brook, New York 11794, United States

4.Mitsubishi Chemical Corporation, Science & Innovation Center, 1000, Kamoshida-cho, Aoba-ku, Yokohama 227-8502, Japan

5. Department of Chemistry, Nova Southeastern University, Fort Lauderdale, Florida, 33137, United States
6. Center for Advanced Microscopy and Materials Analysis, University of Connecticut, 25 King Hill Rd., Storrs, CT 06269, United States

7. Department of Chemical Engineering, Columbia University, New York, New York 10027, United States

8. Center for Functional Nanomaterials, Brookhaven National Laboratory, New York 11973, United States

9. National Synchrotron Light Source II, Brookhaven National Laboratory, Upton, New York 11973, United States

10. Chemistry Division, Brookhaven National Laboratory, Upton, New York 11973, United States

Abstract

Atomically dispersed catalysts have drawn great interest lately, as they showcase a high density of active sites, selectivity, and high turnover frequencies in oxidation chemistry due to labile oxygen activation. In contrast, the applications of these catalysts have lagged in reduction reactions due to the ambiguity caused by the sintering and restructuring of active sites. To bridge this gap, the evolution of Pt^{4+} isomorphically substituted into an octahedral molecular sieve structure (OMS-2) under reductive conditions was correlatively characterized using multiple in-situ analytical techniques such as ambient pressure X-ray photoelectron spectroscopy, environmental transmission electron microscopy, and solid-state nuclear magnetic resonance. The surface dynamics of the Pt single atoms were revealed during the Reverse Water Gas Shift (RWGS) reaction, where the active sites were identified as two-coordinated platinum single atoms. Under reaction, we show nonbinding atoms adjacent to the single atoms restructured the motif of the single atoms to Pt^{2+} via ion mobility of potassium, increasing the activation energy by 25.6 kJ/mol. This work also highlights the potential for increased stability of the single atom sites via isomorphic substitution of the metal oxide support, since the Pt-OMS-2 catalyst retained activity for about 33 hours before deactivation, after which nanoparticles were observed in TEM images. This work offers a new perspective in single atom synthesis using the metal oxide as the host for the single atom site, instead of adatoms on the surface

Introduction

Atomically dispersed catalysts have garnered attention due to their high activity, high dispersion, and good stability in oxidation reactions [1-8]. Such single atom catalysts have been suggested as potential

candidates for bridging the material gap to create green pathways for industrial reactions, such as methane oxidation to methanol, N_2 fixation, and CO_2 reduction [9-11]. However, single atoms in their current form are not utilized in reduction reactions involving hydrogen due to their ease of agglomeration in reductive environments [12,13]. This challenge is less apparent in single atom oxidation reactions due to higher oxygen coordination. Additionally, due to the mobility of platinum single atoms in a reductive environment, ambiguity arises regarding the active site, specifically whether agglomerated nanoclusters drive the chemistry or whether single atoms are responsible for the reaction. Furthermore, is the platinum single atom a $Pt^{2+}O_x$ environment, or do these platinum single atoms take different coordination in reductive environments?

To optimize the stability of platinum single atoms in reductive environments, the knowledge gap regarding the dynamics of single atoms in reduction reactions must be addressed, primarily whether the single atoms are active or agglomerate into active nanoparticles [14-20]. Moreover, it is unclear which single atom motif is preferable for reductive catalysis applications[6,21]. While X-ray absorption fine structure (XAFS) and infrared spectroscopies have been particularly insightful for detecting the average structures of metal species under reaction conditions, there is a need for complementary in-situ experiments. Specifically, environmental transmission electron microscopy (E-TEM) and ambient pressure X-ray photoelectron spectroscopy (AP-XPS) have been used to directly probe the agglomeration and electronic configuration of the single atom species as a reaction occurs[22]. Here, we use these in-situ analytic techniques to correlatively understand the factors influencing SAC sintering under reducing reaction conditions.

chose octahedral molecular sieves, OMS-2 (α-MnO_2), as a catalyst support amenable to EXAFS, E-TEM, and AP-XPS studies. OMS-2 has historical ties to industry, as companies have dredged the ocean floors to capture this material for catalytic and adsorptive processes. The hydrogen ion concentration, paired with the abundance of shark teeth and cetacean ear bones, can lead to active nucleation sites[23]. OMS-2 has also become an emerging support for single atom catalyst in oxidation reactions[24-28]. This is due to OMS-2 having a high density of defects due to the mixed valence allowing to stabilize single atom sites preventing sintering[24, -28]. OMS-2 has an advantage of high oxygen defects that can promote reduction reactions with isomorphic substitutions leading to increased stability under reducing conditions in single atom studies[29-,32]. However, in these studies these single atoms site have shown sluggish kinetics[31].

OMS-2 has several technical advantages, such as a 1-D morphology with a flat surface, which increases the sensitivity in experiments such as E-TEM. Such rods permit the use of grazing angle techniques, such as polarized modulated infrared reflection absorption spectroscopy (PM-IRRAS), to enhance the contrast and increase the signal-to-noise ratio in XPS due to morphology.

Additionally, all the manganese atoms are equivalent, allowing for advanced characterization studies. Platinum was used due to its high Z-number, diamagnetic nature, and high isotopic abundance, enabling us to apply solid-state nuclear magnetic resonance (ssNMR) to these samples. ssNMR allows us to study an important issue in single atom catalysis by examining all the platinum atoms and differentiating them, compared to a local environment such as TEM methods[33]. The Reverse Water Gas Shift (RWGS) reaction was used to probe the catalyst under reduction conditions due to the reaction's relatively simple nature and compatibility with in-situ measurements[34,35].

In this study, two MnO_2 samples were prepared with single atoms of platinum isomorphously substituted into the manganese sites. We conducted multimodal, correlative studies, and kinetic analyses to identify the active sites and probe their evolution under dynamic reaction conditions. After synthesis, platinum substitutes the manganese site to create a six-coordinated platinum single atom site with an oxidation state of 4+, which, under reductive environments, rapidly forms a near neutral Pt species. In the literature two-coordinated Pt[21] has been proposed. This species was found to be highly active for RWGS with high equilibrium conversion rates and methanol production at higher pressures with a yield of 1.4 mmol g^{-1} h^{-1}

and 10% selectivity at 200 °C. During the reaction, the support surface dynamics play a role in the stability of the single atom, as lattice reconstruction in the support is attributed to a change in the near neutral platinum species towards a $Pt^{2+}O_x$ system. Our study suggests that Pt^{2+} has a role in the deactivation of the catalyst at high pressures, dropping the selectivity towards methanol. In addition to this, our study shows the effect of long-range perturbation of the support on the atomically dispersed catalysts motif which is strongly correlated to the activity of the catalyst.

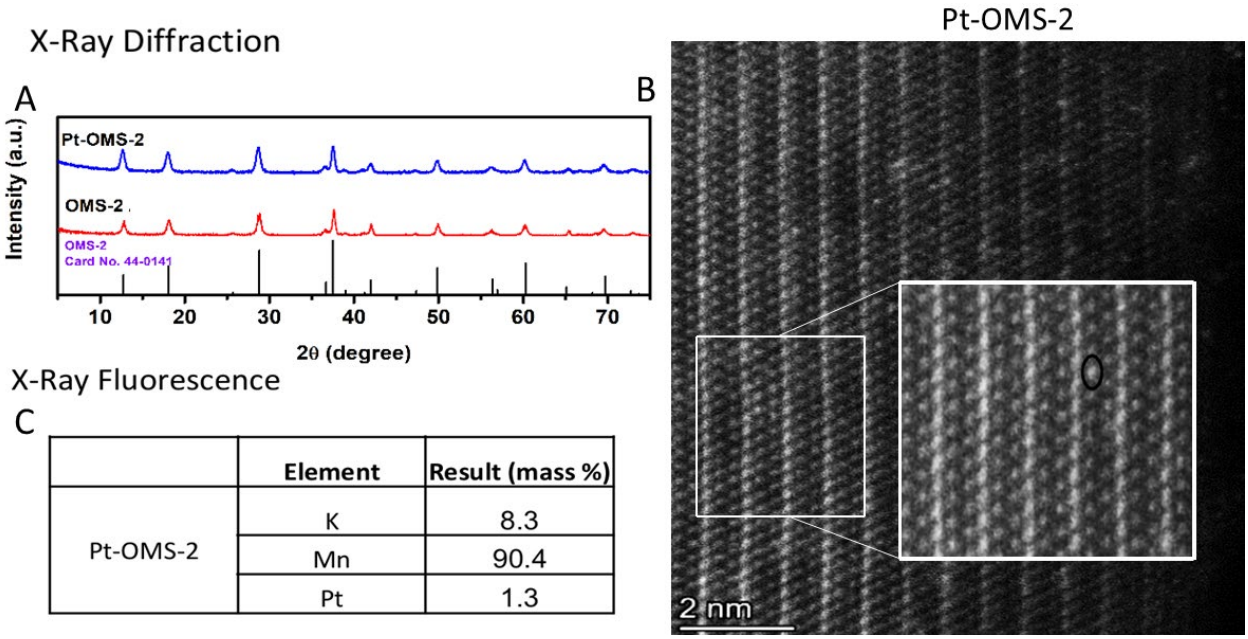

X-Ray Fluorescence

C

	Element	Result (mass %)
Pt-OMS-2	K	8.3
	Mn	90.4
	Pt	1.3

Fig. 1 (A) XRD patterns of the OMS-2 and Pt-OMS-2 samples. (B) STEM imaging of the Pt-OMS-2 (100) zone axis aligned via electron diffraction; the atom circled in black refers to a platinum atom in a Mn column. (C) Tabulation of the XRF results of the Pt-OMS-2.

Structural studies

X-ray diffraction (XRD) was used to determine the phase of the synthesized MnO_2 and the changes after platinum loading. The XRD pattern confirms the formation of the α-MnO_2 structure, i.e., octahedral molecular sieves (OMS-2). After platinum addition via Strong Electrostatic Adsorption, no change was observed in the pattern, indicating that the OMS-2 structure is preserved[36]. No additional peaks were identified, suggesting a high dispersion of platinum throughout the sample.

Complementary to the XRD results, X-ray fluorescence (XRF) was used to measure the platinum content on the OMS-2 sample, which is ~1.3 wt.%, indicating a high percentage of platinum addition. TEM measurements were performed to visualize the platinum sites and probe the platinum-manganese interface. The manganese atoms were aligned to the (100) planes, which are the most thermodynamically favorable facets for platinum to occupy, based on theoretical studies[37]. The micrographs indicate platinum isomorphically substituted for manganese in the lattice, which can be elucidated from the electron density of the atoms, appearing as brighter spots compared to the other atoms in the columns, and profile plots confirm this (Fig. S1). In (Fig. S2) there are no observable clusters, indicating a high degree of atomic dispersion.

A new sample was introduced to compare the cation effects on the platinum active sites, Na-OL-Pt (octahedral-layer MnO_2). This layered structure traps cations in the subsurface, preventing alkali metal ions from migrating to the surface[38]. Due to both catalyst expressing a high density of flat terrace (100) planes of

MnO_2 and their morphologies, both samples have platinum species that will have a similar environment, permitting a direct comparison (Fig. S3)[37]. XRF experiments showed that the platinum loading is comparable, with a Pt loading of 1.0% (Table S1), and no observable clusters (Fig. S4).

Ex-situ X-ray absorption near-edge structure (XANES) spectroscopy was used to elucidate the electron density of atomically dispersed platinum. The intensity of the XANES data in the main absorption edge region, also known as the white line, is related to the effects of the electron-withdrawing groups surrounding the platinum. Such experiments yield a strong white line, indicating electron deficiency with Pt-Na-OL and Pt-OMS-2.

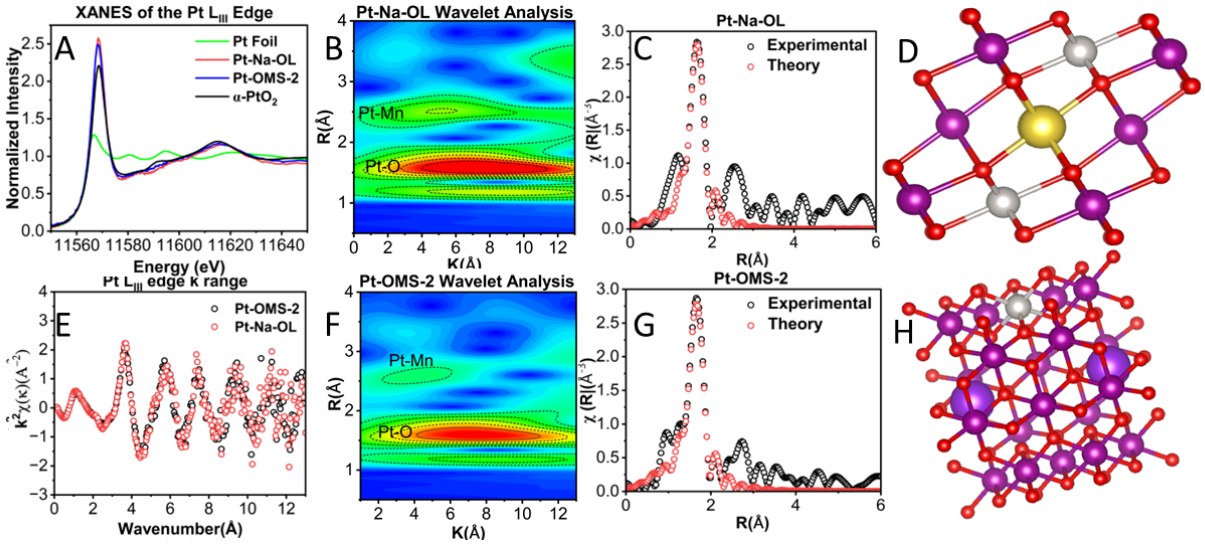

Fig. 2 (A) XANES region of the X-ray absorption coefficient of the Pt-OMS-2 and Pt-Na-OL. (B) Wavelet transform plot for the Pt-Na-OL. The parameters used for the wavelet plot was a k-range of 2.5-13 Å^{-1}, with a RBKG of 1.2 Å^{-1}. (C) Fourier transform magnitudes of the k^2-weighted EXAFS data and fit of the Pt-Na-OL. The k-range and R-range for the fit were 2.5-13 Å^{-1} and 1.3-2.3 Å, respectively. (D) Theoretical structural model used to generate FEFF calculation for Pt-Na-OL where the purple atoms represent manganese, the red atoms represent oxygen, the gold atoms represent sodium, and the silver atoms represent platinum. (Table S2) (E) k^2-weighted EXAFS data in k-space of both Pt-OMS-2 and Pt-Na-OL The k-range and R-range for the fit were 2.5-13 Å^{-1} and 1.3-2.3Å, respectively. (F) Wavelet transform plot for the Pt-OMS-2. The parameters used for the wavelet plot was a k-range of 2.5-13 Å^{-1} with a RBKG of 1.2 Å^{-1}. (G) Fourier transform magnitudes of the k^2-weighted EXAFS data and fit of the Pt-OMS-2. (H) Theoretical model used to generate FEFF calculation for Pt-OMS-2 where the purple atoms represent manganese, the red atoms represent oxygen, the blue atoms represent potassium, and the silver atoms represent platinum[39] (Table S3).

Shell	CN	R(Å)	ΔE_0 (eV)
OMS-Pt-O	5.3 ± 0.9	2.03 ± 0.01	14.1 ± 2.0
OL-Pt-O	5.2 ± 0.7	2.01 ± 0.01	10.2 ± 1.8

Table I EXAFS analysis results of the Pt-OL and Pt-OMS-2, CN refers to the coordination number, R(Å), refers to the interatomic distance of the atomic pairs. The ΔE_0 refers to the correction to the photoelectron

energy origin. The σ^2 (the mean squared disorder of bond length) was found to be consistent with zero, within uncertainties, for both samples.

Both samples' Extended XAFS (EXAFS) spectra were fitted with Artemis software to resolve the coordination numbers and bond lengths of Pt nearest neighbors. Based on the TEM studies, a model in which platinum is isomorphically substituted into MnO_2 was chosen for both samples to generate theoretical EXAFS spectra[39].To obtain the bond length and coordination number, these theoretical spectra were fitted to the experimental spectra and these results are given in Table I. The theoretical fit for the Pt-O yielded coordination numbers of 5.2±0.7 and 5.3±0.9 for the Pt-OMS-2 and Pt-Na-OL, respectively. Furthermore, the interatomic distance of both Pt-O bonds is 2.01±0.01Å and 2.03±0.01Å consistent with both PtO_x and atomically dispersed platinum[40-42].

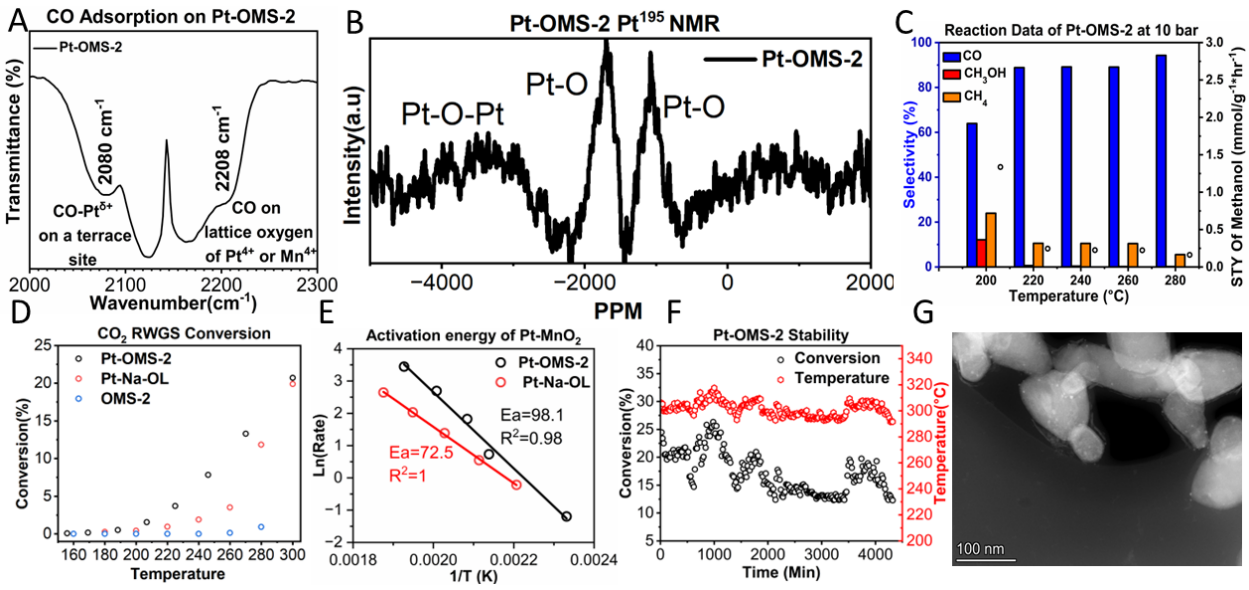

Fig. 3 (A) CO adsorption characteristics of the atomically dispered Pt sites on OMS-2 catalysts through a transmission IR spectrum. (B) ssNMR of the Pt-OMS-2 showed no Pt-O-Pt binding indicating no clusters. (C) RWGS conversion performance of the Pt-OMS-2 at 10 bars, showing non-negligible methanol yield at 200 ºC. (D) Reverse water-gas shift (RWGS) conversion of CO_2 to CO over OMS-2, Pt-OMS-2, and Pt-Na-OL catalysts. (E) Arrhenius plots extracting the apparent activation energies for the Pt-Na-OL and Pt-OMS-2 in the RWGS reaction. (F) RWGS conversion performance of the Pt-OMS-2 catalysts throughout 72 h. (G) STEM imaging of the Pt-OMS-2 after the stability study showing filamentous layers around the MnO_x with Pt nanoparticles.

However, the need for a custom CIF file to generate this fit, as bulk PtO_x could not be fitted to the experimental data signaling that Pt is adjacent to Mn sites. Due to these results PtO_x can be ruled out in this system.

Identification of the active site $Pt^{\sigma+}$, reactivity, and stability.

The electronic density of the isomorphically substituted platinum was probed by CO. The CO peak that appears at 2080 cm^{-1} is correlated with a near neutral atomic platinum peak with two-fold coordination with oxygen on a terrace [21,43]. This indicates that there are platinum adatoms on the (100) facets, which are flat terrace planes. These two-coordinate features are most likely the active site under reaction conditions,

implying that platinum reassembles during the reaction. In addition to this peak, a peak at 2208 cm^{-1} appears, related to a CO-Pt^{4+} adduct, which is the same species that appears in EXAFS as octahedral lattice-bound Pt^{4+} [44].

Solid-state ^{195}Pt NMR (Nuclear Magnetic Resonance) was used to understand the interactions between Pt atoms and confirm atomic dispersion. NMR spectra indicate platinum has two peaks around -2000 ppm, typically assigned to Pt-O bonding [45,46]. The peaks are sharp, indicating that the platinum is diamagnetic, consistent with the octahedral Pt^{4+} motif. Pt-O-Pt exhibits a sharp peak at -4000 ppm [47]. This peak disappears when correcting for first-order phasing, indicating that platinum dimers or clusters do not exist in the sample.

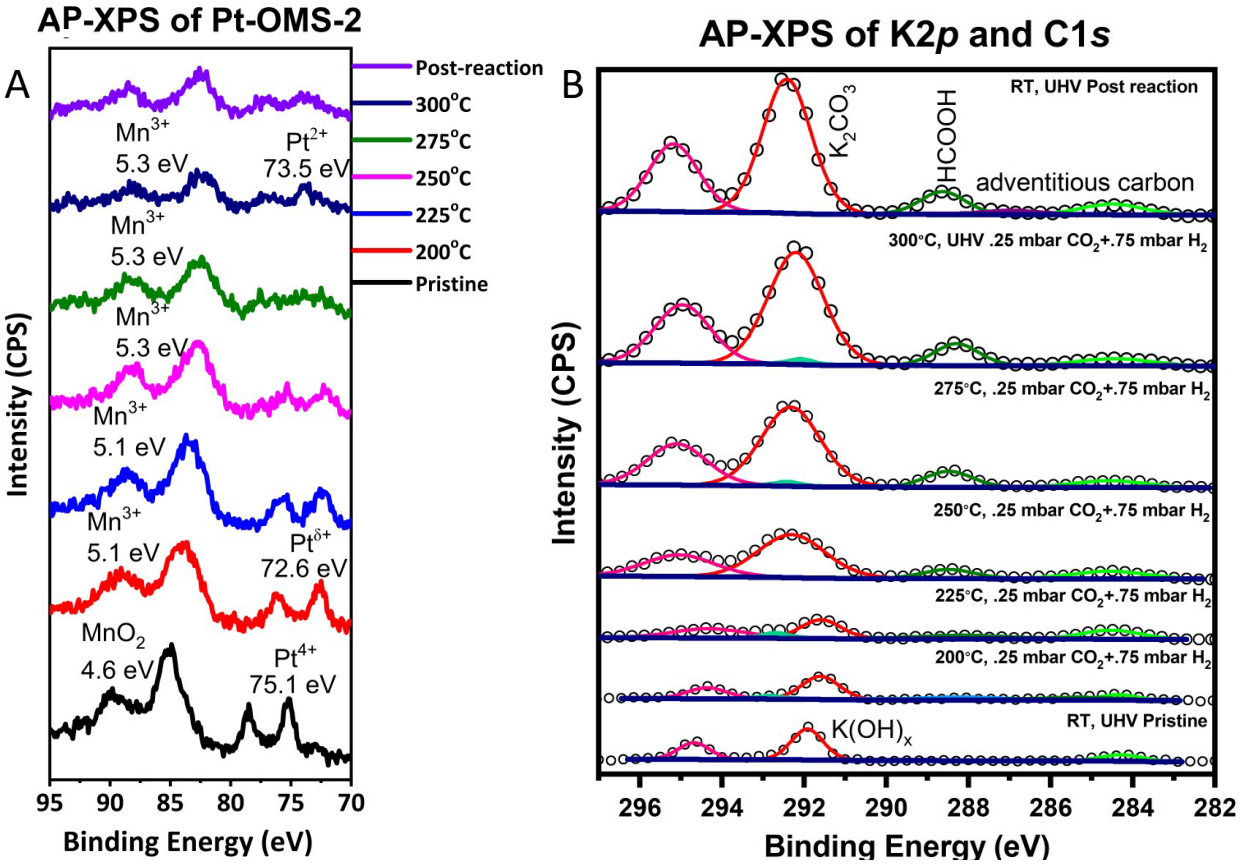

Fig 4 (A) AP-XPS data of Mn 3s and the Pt 4f core levels under dynamic reaction conditions of 0.25 Torr of CO_2 and 0.75 Torr of H_2 co-dosed. (B) AP-XPS of K 2p and the C 1s core levels under dynamic reaction conditions, showing migration of potassium on the surface at 1 torr. O1s spectra and XPS curve fitting details can be seen in (Fig. S5-9) and (Table S4-13).

Reaction studies were conducted on the manganese catalysts. OMS-2 shows low reactivity toward the RWGS reaction, with maximum conversion of CO_2 reaching 0.9% at 280 °C. When compared to the isomorphically substituted platinum system (Pt-OMS-2), a conversion of ~13% and an increase in the spacetime yield of about 27 times the amount of OMS-2 at maximum temperature are observed, with the Pt-OMS-2 producing a spacetime yield of 82.4 mmol g^{-1} hr^{-1} of CO, was observed.

When compared to the Pt-Na-OL sample, the Pt-OMS-2 has a higher conversion at lower temperatures until equilibrium is reached, while maintaining 100% selectivity at all temperatures (Fig. S10). However, when normalizing, platinum Pt-Na-OL has an increased TOF value (Table S14). The activation energy was

elucidated from an Arrhenius plot generated by the reactivity data. Pt-Na-OL has a lower activation energy than the Pt-OMS-2 sample by 25.6 kJ/mol. This implies a cation effect, or a restructuring of the platinum atom sites, as both platinum atoms are in similar chemical environments. The main difference in these catalysts is that sodium is trapped in the Pt-Na-OL, whereas potassium can migrate to the surface in the Pt-OMS-2.

Reactivity studies were conducted at 10 bars for the Pt-OMS-2 and OMS-2 sample to study the pressure effect on products (Fig. S11). The selectivity of the catalyst significantly changes, with 10% selectivity at 200 °C and an STY of 1.3 mmol g^{-1} hr^{-1}. However, this selectivity drops as the temperature increases. A similar trend is observed for methane, suggesting similar active sites at the beginning of the reaction.

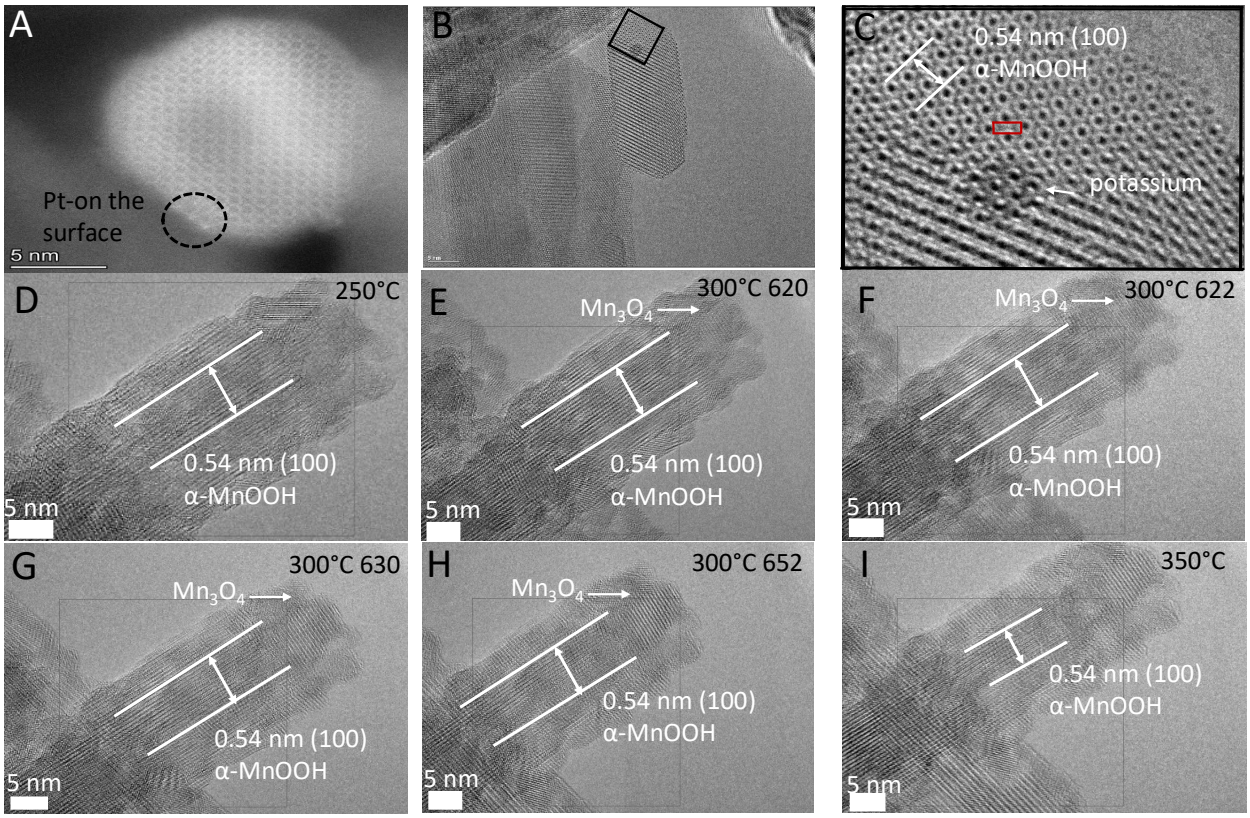

Fig. 5 (A) STEM imaging of Pt-OMS-2 showing Pt on the surface with the (010) facet aligned to show the tunnels. (B) E-TEM image of the Pt-OMS-2 after reaction with no beam during the reaction. (C) Zoomed-in image of the 1X2 tunnels typically seen in Ramsdelite. (D) E-TEM image of Pt-OMS-2 under reaction conditions at 250 °C. (E) E-TEM image of Pt-OMS-2 under reaction conditions at 300 °C at 6 torrs. (F) E-TEM image of Pt-OMS-2 under reaction conditions at 300 °C 2 frames after E. (G) E-TEM image of Pt-OMS-2 under reaction conditions at 300 °C 10 frames after E. (H) E-TEM image of Pt-OMS-2 at under reaction conditions at 300 °C 22 frames after E. (I) E-TEM image of Pt-OMS-2 under reaction conditions at 350 °C .

To produce methane with the large number of electrons needed, a metallic active site is likely.

Long-term reactivity studies were performed. Na-OL is not stable in acidic media (CO_2) and will decompose into β-MnO_2, due to production of carbonic acid, which will convert the Na-OL, leading to instability. Due to this, the focus of the study was on Pt-OMS-2 due to increased stability in acidic media. A 72-hour stability test was performed to

track the change in activity over a long period. The stability study of the Pt-OMS-2 starts with slight deactivation due to not being at a steady state, then holds its activity for 8 hours. Temperature fluctuations then appear to cause a loss in activity, with the initial activity still holding at 2000 min. After 2000 min, signs of sintering are observed as the temperature returns to the initial value. However, the conversion is significantly hindered by a 25% drop-in activity. After the stability test, XRD patterns, and TEM Micrographs were taken to study the evolution of the Pt-OMS-2 after 72 hours (Fig. S12). These micrographs suggest that platinum leaves the lattice and forms platinum nanoparticles on the surface. In addition, an overlayer appeared on the manganese. These data suggest an element close to Mn in the periodic table. However, energy-dispersive X-ray spectroscopy (EDX) experiments of Fig 2G, which were used to identify the layer's chemical composition, did not yield any definitive data. The layer is likely potassium, manganese, or both.

H+/K+ exchange and isotopic mechanistic studies

AP-XPS was employed to monitor the oxidation states to understand how the electronic properties of the catalyst change under reaction conditions. In addition, XPS probes the surface of the catalyst, making it sensitive to electronic changes.

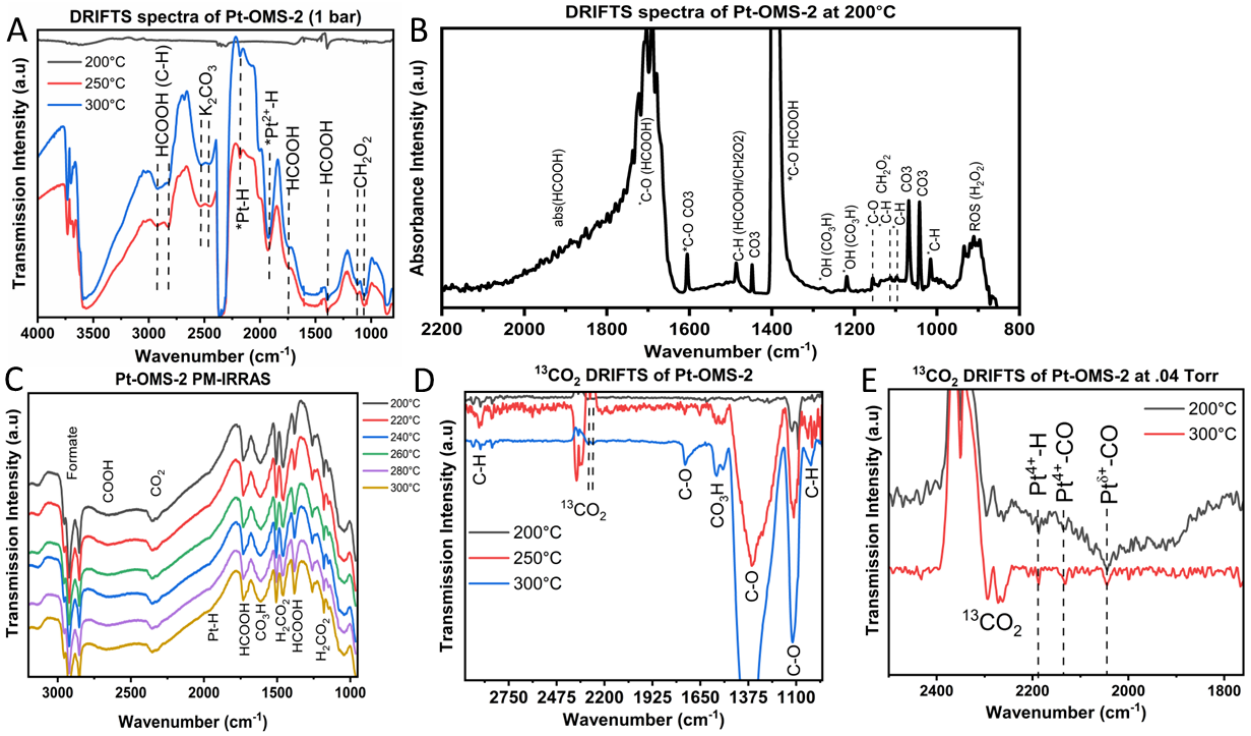

Fig. 6 (A) DRIFTS spectra of the Pt-OMS-2 and 30 sccm of a 3:1 H_2 and CO_2 mixture at 200 °C,250 °Cand 300 °C at atmospheric pressure. (B) DRIFTS of the Pt-OMS-2 at 200 °C and 30 sccm of a 3:1 H_2 and CO_2 mixture before potassium leaves the tunnels at atmospheric pressure. (C) PM-IRRAS spectra of the Pt-OMS-2 at 1 mbar with a 3:1 H_2 and CO_2 mixture Transmission IR spectra of Pt-OMS-2 under $^{12}CO_2$ and H_2 1:3 ratio at 0.04 torr. (D)Transmission IR spectra of Pt-OMS-2 under $^{13}CO_2$ and H_2 1:3 ratio at 0.04 torr. (E) Baseline Corrected Transmission IR of the Pt-OMS-2 of the carbonyl region at 0.04 torr with a 3:1 H_2 and $^{13}CO_2$ mixture (Fig. S13).

When the catalyst was in its pristine form, the platinum oxidation state was 4+, indicated by the 75-eV peak for the Pt $4f_{7/2}$ in Figure 4a[48]. After the reaction started, the platinum was reduced to a near neutral state that has also been referred to as Pt $(OH)_2$, which is active during the reaction, agreeing with the CO-IR studies[21,43 49,50,51]. Manganese shifts to a 3+ state based on the orbital splitting under these same reaction conditions[52]. When the temperature increases to 250°C, the intensity of the potassium increases and shifts to higher binding energy, indicating a change in the potassium.

One explanation for this behavior is that potassium migrates to the surface and forming K_2CO_3. Coinciding with this change is the shrinking signal of platinum, implying a reconstruction of the catalyst under reaction conditions. Pt is displaced from the catalyst surface. At the final temperature, platinum oxidizes to 2+, which is related to the $Pt^{2+}O_x$ after reconstruction[53]. After the reaction was concluded, another spectrum was acquired to check for metastable phases. From this scan, there were no changes. In Fig. 4B the C 1s could not yield detailed information as the peak was too broad to fit. However, at 288 eV formic acid appears in the XPS possible suggesting an important role in the reaction. O 1s was similar in that key intermediates could not be seen (Fig. S5-9). However, as the temperature increases the peak at 530 eV increases which is due to OH^- until the OH^- peaks is as intense as the lattice oxygen. This is typical in oxyhydroxide systems possibly signaling that an oxyhydroxide is forming in-situ.

To explore the reconstruction of the catalyst during reaction conditions, E-TEM was used to monitor the catalyst. STEM (Scanning Transmission Electron Microscopy) was used to identify the platinum location, confirming that platinum is on the surface (Fig. 5A). To identify the effect of the beam, experiments were first conducted with no beam under reaction conditions as seen in Fig. 5 B,C. These conditions show MnOOH forms in situ, which is evident from the 1x2 tunnel formation. The Ramsdellite phase (1x2 tunnel) is typically synthesized by hydrogen ion replacement in the tunnels[54]. This suggests an ion replacement of potassium and hydrogen. In addition, in-situ heating was performed to test the effect of just heat, as seen in (Fig. S14).

The catalyst was then tested under reaction conditions to examine the stability of platinum under reaction at 250 °C, See Fig. 5D. A change to the 1x2 Ramsdellite structure is observed indicating that H_2 has exchanged with K^+ to make H^+ in the tunnels. As the temperature was increased to 300 °C (Fig. 5 E, D, F, H) the formation of Mn_3O_4 is observed at the tip of the rod. Under reaction conditions, platinum did not agglomerate until after the experiment, when the beam current was increased. To show that the platinum was stable beyond the dynamic region of the study we increased the temperture to 350°C and still there was no platinum aggregation. The observation seen in the E-TEM is in line with our reactivity study, as sintering appears after 33 hours.

To gain further mechanistic understanding of the catalytic mechanism, we used a variety of infrared techniques such as DRIFTS, Transmission Infrared Spectroscopy (TIR), and PM-IRRAS. In addition, isotopic labeling was used to determine the functional groups of the IR bands. From the DRIFTS spectra in Fig. 6 A, B, at 200°C in Figure B, there are several IR bands. The bands at 1140 cm^{-1}, 1180 cm^{-1}, and 1484 cm^{-1} are typically attributed to CH_2O_2 (Dioxymethylene), a key intermediate in methanol synthesis[55]. In addition to these peaks, a peak around 1750 cm^{-1} is observed, which is typically attributed to formic acid (HCOOH)[56]. Furthermore, in Fig. 6B also shows the HCOOH peak via a broad shoulder appearing at the peak at 1760 cm^{-1}, the broadness of the shoulder is typically indicative of hydrogen bonding, via high surface coverage of HCOOH. In Fig 6 A when the temperature was increased to 250°C and 300°C a unique feature appears in the DRIFTS data at 2463 cm^{-1} and 2550 cm^{-1}. These peaks are typically assigned to potassium carbonate suggesting that potassium migrates to the surface and binds to CO_2[57]. When this occurs at 250°C, a new peak appears at 1960 cm^{-1}, which is related to Pt^{2+} hydride formation, showing a connection to the Pt^{2+} system and the restructuring of the catalyst[58].

Because this sample is a molecular sieve, polarization-modulated IRRAS was used to determine surface

intermediates in Fig. 6 D. The angle of the polarizer was changed to probe just the surface of the catalyst and ignore the tunnels. The same intermediates were formed on the surface of the catalyst. Dioxymethylene and formic acid are still formed, as seen in the DRIFTS spectra. New peaks at 1520 cm^{-1} and 1560 cm^{-1} appear, which, in previous experiments, have been assigned to bicarbonate species[59]. A peak in the region of 2700 cm^{-1} is where potassium carbonate appears but the peak shape is not a doublet which rules out K_2CO_3. For this reason, this band is assigned to COOH[60].

To determine the functional groups of the intermediates, $^{13}CO_2$ FTIR experiments were implemented, as seen in Fig. 6 B, C. From the experiments, the identity of the intermediate CH_2O_2 is supported by the shift seen in the peaks near 1080 cm^{-1} and 1120 cm^{-1}, indicating that these peaks reflect C-H and C-O, respectively[55]. Peaks at 1514 cm^{-1} and 1560 cm^{-1} are seen which correlate to bicarbonate. These peaks did not shift, indicating they are not related to carbon bonding[59]. Leading us to believe these bands are assigned to the OH of bicarbonate.

The carbonyl region in Fig. 6E shows the shift in the single atoms from $^{13}CO_2$, which can be used to confirm in situ observation of active sites. The peak at 2208 cm^{-1} matches with the expected shift from ^{12}C to ^{13}C with the peak at 2129 cm^{-1} in Fig. 6E, confirming that the CO-adduct of the Pt^{4+} substituted atom is still present during the reaction. In addition, a new peak appears at 2184 cm^{-1}. This peak was also seen in the DRIFTS spectra in Fig. 6A. This peak did not shift indicating that carbon is not responsible for this peak. This peak is assigned to Pt^{4+}-H^-, as this peak does not contain carbon. The peak at 2040 cm^{-1} does not match the previously seen peak at 2080 cm^{-1}, but if considered as a dicarbonyl, this peak is an exact match. Therefore, the peak at 2040 cm^{-1} is assigned to a near neutral platinum with bound to two carbon monoxides.

Discussion

From the above data, such as XRD, TEM, ssNMR, XANES, and EXAFS, platinum is atomically dispersed on the (100) facets of the OMS-2 structure. XPS, XANES, and EXAFS data indicate that the single atoms are synthesized with a Pt^{4+} oxidation state and a coordination number of 6, implying an octahedral platinum site. When comparing the EXAFS data in r-space and k space (Fig. S15) of Pt-OMS-2 and Pt Na-OL, the trends in the second neighbor region (3-5 Å) do not follow the pattern of PtO_2, indicating that the local structure of Pt is different in the Pt-Na-OL and Pt-OMS-2 samples than PtO_2. This argument is supported by TEM data in Fig. 1B studies that show an isomorphic substitution, as well as ssNMR showing a diamagnetic Pt species.

This octahedral platinum site may be inactive, as AP-XPS shows that these substituted platinum atoms (Pt^{4+}) reduce under reaction conditions to form ($Pt^{\sigma+}$). This reduced species is consistent with a surface-bound and two-coordinated system on terraced sites which is supported by CO-IR experiments as well as in IRRAS experiments and confirmed with C^{13} DRIFTS[21,43]. However, Pt^{4+} is still observed during reaction conditions in in-situ IR experiments and is seen to generate H^-, which could work in tandem with $Pt^{\sigma+}$ sites and aid in the catalytic reaction. From these experiments, the active site at low temperatures is likely $Pt^{\sigma+}$, which can be assisted by Pt^{4+}. Similar sites are likely involved in methanol synthesis.

When the temperature increases in AP-XPS Fig. 4A and IR Fig. 6 A, E the $Pt^{\sigma+}$ sites disappear, while potassium migrates to the surface (see Fig. 6A and Fig. 4 A, B) and a new site forms that is consistent with $Pt^{2+}O_x$. In the IR experiments Pt^{2+} hydrides are also formed when the potassium migrates to the surface (Fig. 6A). This implies that potassium (K^+) may exchange with hydrogen (H^+), restructuring the platinum site to Pt^{2+} which then bonds with H^-. This mechanism is consistent with a heterolytic hydrogen activation mechanism. In addition to this information from AP-XPS and IR E-TEM show the formation of MnOOH which is a structure that forms when hydrogen is exchanged with the potassium in the tunnels. This phenomenon may also explain the 10 bar reaction data and would imply that $Pt^{\sigma+}$ is an active site for methanol synthesis, which then restructures into Pt^{2+}, promoting the RWGS and agglomeration, as observed

in stability studies with a decrease in conversion over time. However, the pressure limits in experiments prevent us from probing the reaction at 10 bars.

This phenomenon may also explain the layered structure seen in the STEM data Fig 2G after the 72-hour stability study. This suggests that the layer structure involves K_2CO_3 forming on the catalyst's surface. This is consistent with the AP-XPS Fig. 4B, as well as the IR experiments Fig.6A, which show the formation of K_2CO_3 at 2600 cm^{-1} [57].

IR experiments strengthen the argument for an active Pt^{2+} site since a peak at 1960 cm^{-1} is observed which we attribute to as Pt^{2+} hydride in both the DRIFTS and IRRAS[58]. Pt^{2+} carbonyls were not seen in IR experiments, perhaps due to fast kinetics, which would obscure the peak in IR or Pt^{2+} can`t bind the carbonyl. These hydride peaks appear when potassium migrates to the surface and is congruent with our hypothesis that surface reconstruction can cause dynamic changes to single-atom structures (Fig. S16). Additionally, a catalytic mechanism was proposed, as we see in low temperatures regimes that dioxymethylene is formed via IR spectroscopy. When the temperature increases, it is seen that this peak disappears and formic acid peaks grow we attribute this to tautomerization of DOM into formic acid. Then Formic acid after formation decomposes into CO + H_2O. These intermediates would explain why methanol forms at higher pressures, as the higher pressure may allow for further hydrogenation of dioxymethylene/formic acid into methanol.

In conclusion, Pt single atoms substitute the manganese atoms in OMS-2, as determined from EXAFS, NMR, IR, and TEM experiments. From in-situ experiments, these Pt^{4+} substituted sites transform to a $Pt^{\sigma+}$ species, which, at higher pressures, favors methanol synthesis; then these sites transform into a Pt^{2+} species, which promotes an RWGS pathway. This switch in the catalyst is intrinsically tied to a restructuring of the support from MnO_2 to MnOOH due to potassium ion exchange with a proton in the tunnels. When ion mobility was reduced by introducing a layer structure (Na-OL), a distinct change in performance was observed, with a lower activation energy and a higher rate of catalytic turnover per metal site. This shows that $Pt^{\sigma+}$ sites are direct active sites for reductive reactions. The two-coordinated platinum systems may be more stable than initially thought, with no evidence of direct sintering of this site. Instead, an intermediate step occurs in which $Pt^{\sigma+}$ transitions to Pt^{2+} and sinters over time. This suggests a potential strategy to stabilize these atomically dispersed platinum sites by preventing or reducing the transition into $Pt^{2+}O_x$. The IRRAS experiments with labeled CO_2 also provide direct evidence that single atoms are directly involved in the catalytic pathway and suggest a possibly viable mechanism for CO_2 hydrogenation toward the formation of alcohols

Methods

Catalyst Synthesis. All reagents were purchased through Sigma Aldrich and used without further purification. The synthesis of OMS-2 was started by mixing fourteen moles of manganese sulfate, twenty-one moles of potassium persulfate, and twenty one moles of potassium sulfate in sixty milliliters of water and mixing until homogenous. After thirty minutes, the solution was heated for two days at 200 °C in an autoclave inside a ventilated oven. The resulting material was washed using DDI water until the pH was neutral and placed in an oven to dry overnight at 120 ºC. This material was used as the Octahedral Molecular Sieves (OMS-2).

Na-OL Synthesis. All reagents were purchased through Sigma Aldrich. The synthesis was started for the layered manganese oxide by adding 3.0 g of $NaMnO_2$ into 50 mL of water in a 250 mL beaker. After this a 1.4 M solution of glucose in water with a volume of about 20 mL was added into the NaMnO2 beaker under fast stirring for about a minute, then was left static producing a reddish-brownish sol. After the temperature of the beaker returned to room temperature the sol was then dehydrated in a drying oven at 110ºC, and every 15 mins water was removed from the beaker. The

resultant material was then placed inside a muffle furnaced and calcined at 400 ºC to produce a puck of manganese. The puck was cooled and then ground in a mortar and pestle to produce a powder which was then placed in 100 mL of water overnight to remove unreacted products. This solution was then vacuum filtered and the powder was washed an additional three times. After this powder was dried in static air the powder was again placed in a drying oven at 110ºC to remove all water. Platinum was added to this solution using the Strong Electrostatic Adsorption method

Platinum adsorption. The platinum single atoms were synthesized on the manganese oxide supported catalyst by strong electrostatic adsorption. 1 g of manganese oxide is introduced to a vial with 2 mL of ammonia hydroxide and 10 mL of ethanol. After the dispersion of the manganese oxide, 1 mL of platinum tetraamine nitrate was added to the solution; the vial was then placed on an orbital shaker for 60 minutes. The solution was then filtered and calcined at 350 ºC for 240 minutes. The platinum weight percent was characterized by X-ray fluorescence spectrometry.

Characterization. XRD-Powder X-Ray Diffraction (PXRD) experiments were performed utilizing a Rigaku Ultima IV diffractometer with Cu Kα radiation (λ = 0.15406 nm). X-ray diffraction (XRD) measurements were collected from 5º–80° 2θ, with a 2.0°/min scan rate. The diffraction patterns were compared with the Joint Committee on Powder Diffraction Society (JCPDS) database.

Transmission Electron Microscopy- A Titan Themis ACEM microscope was used to perform Transmission Electron Microscopy (TEM). Samples were dissolved in ethanol and drop-cast onto lacy carbon-coated TEM grids and then vacuum-dried. DENS Wildfire holder was used for E-TEM experiments with the sample drop cast onto DENS Thurhole chips. Hydrogen and carbon dioxide were introduced at a 3:1 ratio at five torrs, then the holder was heated to 300 ºC. Images were taken over 8 hours.

Ambient pressure X-ray Photoelectron spectroscopy- AP-XPS data were collected at the Center for Functional Nanomaterials with a laboratory-based APXPS instrument[44]. A 300 micron aperture was used in the analysis chamber to facilitate a differentially pumped electrostatic lens system and a SPECS PHOIBOS NAP 150 hemispherical analyzer. A monochromatic photon source was used (Al K_a) which is focused on a ~300 micron diameter spot. The starting pressure of the analysis chamber was less than 5×10^{-9} mbar. Precision leak valves were used to introduce hydrogen and carbon dioxide at a 3:1 ratio with a total pressure of one Torr. An infrared laser was used to heat the sample from the backside with a K-type thermocouple monitoring the temperature. To prepare the samples, a small amount of catalyst was sandwiched between two copper plates and compressed in a hydraulic press to form a thin sample pellet[61].

Diffuse Reflectance Infrared Fourier Transform Spectroscopy- A Nicolet 6700 FTIR and a DRIFTS chamber from Pike Technologies were used to carry out Diffuse Reflectance Infrared Fourier Transform Spectroscopy (DRIFTS) using a ZnSe reaction window with a liquid-cooled MCT detector with 256 scans and 2 cm^{-1} resolution; 30 mg of sample was placed in a crucible and pretreated with flowing argon at 130 ºC for 1 hour in the DRIFTS chamber. The gases (H_2/CO_2/Ar) at 60/30/10 were introduced at thirty sccm, before a steady state was achieved, the background spectra were taken. The temperature was consequently increased with multiple spectra taken over 30 minutes at each temperature.

Transmission infrared spectroscopy- A Bruker 80v infrared spectrometer equipped with a liquid nitrogen-cooled MCT/A detector was used for data collection. A ~50 mg amount of Pt-OMS-2 was placed on a tungsten mesh (75% transmission). After compression in a hydraulic press, the mesh supported thin areas of catalyst within the grid. The tungsten mesh was then mounted onto the holder and placed inside the transmission cell, which is a high vacuum chamber with a base pressure better than 1 x 10^{-5} Torr. Isotopically labeled ^{13}CO and H_2 were then added at a 1:3 ratio to the desired pressure. The sample was heated with a resistance heater, and a background was taken of blank tungsten mesh. The sample was then moved into the beam path, and the data were collected at 200°C, 250°C, and 300°C. For CO experiments, liquid nitrogen was used to cool the sample to below 77 K, and then CO gas was leaked in for data collection.

Polarized Modulated Infrared Reflection Spectroscopy- A Bruker infrared spectrometer with a custom IRRAS setup[44] was used for data collection equipped with the sample environment is a small UHV chamber in the path of the IR beam that exits the spectrometer and is collected with a liquid nitrogen-cooled MCT/A detector that is external to the spectrometer. The Pt-OMS-2 catalyst was prepared by placing 50 mg of catalyst in between two single-crystal Al_2O_3 tabs. This was then forced together with a hydraulic press, and then separated in half. The single crystal Al_2O_3 with Pt-OMS-2 was then placed in the IRRAS and leak values were used to leak in 0.75 mbar of H_2 and 0.25 mbar of CO_2. At UHV conditions (5 x 10^{-9} mbar) and relevant sample temperatures, a background was taken at both 90° and 0° light polarization. The temperature was increased with a halogen bulb, and scans were taken from 200°C to 300°C at 20°C increments. For each temperature, scans were taken with both 0° and 90° light polarizations. The s and p spectra were subtracted at each temperature in post-processing to eliminate gas phase components

X-ray absorption spectroscopy (XAS) measurements were obtained using the 7-BM beamline (QAS) at the National Synchrotron Light Source II of Brookhaven National Laboratory. Ex-situ XAS spectra of the Pt-OMS-2 samples were acquired in fluorescence mode with the energy range optimized for the Pt L_3-edge (11564 eV). The sample was prepared by brushing on Kapton tape and folding the tape over 8-10 times for uniformity. Data processing and analysis were performed using the Demeter package [62].

X-Ray Fluorescence Spectroscopy (XRF)- Elemental analysis and quantification was performed by loading 100 mg of Pt-MnO_2 in a 10 mm ID sample cup. A metal holder was used for sample collection in a Rigaku ZSX Primus IV sequential wavelength-dispersive XRF spectrometer (4 kW Rh anode).

Solid State Nuclear Magnetic Resonance- ssNMR work was done on a Bruker AVANCE III 400 WB (85.7 MHz for 195Pt). Samples were packed in 4 mm zirconia rotors and spun at 7500 Hz. A 7.0 used a 90 degree pulse and a 2 sec recycle delay was used for sample acquisition. A total of 5120 scans were collected.

Methanol synthesis. A horizontal fixed bed reactor of a 1/8" quartz tube in a resistively heated furnace was used to conduct CO_2 hydrogenation reactions. Quartz wool plugs were used to secure 100 mg of the Platinum-Manganese catalyst. The catalyst was used with no pretreatment. An H_2/CO_2 mixture (75%/25%) was introduced at 30 SCCM through the catalyst bed. A ramp rate of 20ºC/min was utilized when heating the samples from 200ºC to 300ºC with triplicate measurements to ensure reproducibility taken every 20 ºC/min. All products were analyzed by Gas Chromatography (GC)

which was calibrated via Calibration gas. The equation determined the CO_2 conversion, TOR, selectivity, and STY Below.

CO_2 conversion (%) $= \frac{nCH4+nCO+nCH3OH}{nCO2\ tot}$

CH_3OH selectivity (%) $= \frac{nCH3OH}{nCO+nCH3OH+nCH4}$

STY of CH3OH $(\frac{mmol\ of\ CH3OH}{g*hr}) = \frac{PPM\ of\ CH3OH*flowrate(SCCM)*Time(Hr)}{mass\ of\ the\ catalyst\ (g)*22400}$

TOR/TOF $(\frac{mol\ of\ CH3OH}{mol(metal)*sec}) = (\frac{mol\ of\ CH3OH}{mol(metal)*3600})$

References

1. Liang, X., Fu, N., Yao, S., Li, Z. & Li, Y. The Progress and Outlook of Metal Single-Atom-Site Catalysis. *J. Am. Chem. Soc.* **144**, 18155–18174 (2022).

2. Li, L., Chang, X., Lin, X., Zhao, Z.-J. & Gong, J. Theoretical insights into single-atom catalysts. *Chem. Soc. Rev.* **49**, 8156–8178 (2020).

3. Beniya, A. & Higashi, S. Towards dense single-atom catalysts for future automotive applications. *Nature Catalysis* **2**, 590–602 (2019).

4. Lu, Y. *et al.* Identification of the active complex for CO oxidation over single-atom Ir-on-MgAl2O4 catalysts. *Nature Catalysis* **2**, 149–156 (2019).

5. Wang, H. *et al.* Migration and aggregation of Pt atoms on metal oxide-supported ceria nanodomes control reverse water gas shift reaction activity. *Communications Chemistry* **6**, 264 (2023).

6. Chen, L.; Unocic, R. R.; Hoffman, A. S.; Hong, J.; Braga, A. H.; Bao, Z.; Bare, S. R.; Szanyi, J. Unlocking the Catalytic Potential of TiO2-Supported Pt Single Atoms for the Reverse Water–Gas Shift Reaction by Altering Their Chemical Environment. *JACS Au* **2021**, *1* (7), 977–986. https://doi.org/10.1021/jacsau.1c00111.

7. Cao, D. *et al.* One-Step Approach for Constructing High-Density Single-Atom Catalysts toward Overall Water Splitting at Industrial Current Densities. *Angewandte Chemie International Edition* **62**, e202214259 (2023).

8. Qiao, B. *et al.* Single-atom catalysis of CO oxidation using Pt1/FeOx. *Nature Chemistry* **3**, 634–641 (2011).

9. Feng, X. *et al.* Hydrogen Radical-Induced Electrocatalytic N2 Reduction at a Low Potential. *J. Am. Chem. Soc.* **145**, 10259–10267 (2023).

10. Sarma, S. C. *et al.* Reaching the Fundamental Limitation in CO2 Reduction to CO with Single Atom Catalysts. *Advanced Functional Materials* **33**, 2302468 (2023).

11. Li, H. *et al.* Selective Formation of Acetic Acid and Methanol by Direct Methane Oxidation Using Rhodium Single-Atom Catalysts. *J. Am. Chem. Soc.* **145**, 11415–11419 (2023).

12. Farnesi Camellone, M.; Dvořák, F.; Vorokhta, M.; Tovt, A.; Khalakhan, I.; Johánek, V.; Skála, T.; Matolínová, I.; Fabris, S.; Mysliveček, J. Adatom and Nanoparticle Dynamics on Single-Atom Catalyst Substrates. *ACS Catal.* **2022**, *12* (9), 4859–4871. https://doi.org/10.1021/acscatal.2c00291.

13. Wang, W.; Wu, Y.; Lin, Y.; Yao, J.; Wu, X.; Wu, C.; Zuo, X.; Yang, Q.; Ge, B.; Yang, L.; Li, G.; Chou, S.; Li, W.; Jiang, Y. Confining Zero-Valent Platinum Single Atoms in α-MoC1−x for pH-Universal Hydrogen Evolution Reaction. *Advanced Functional Materials* **2022**, *32* (12), 2108464. https://doi.org/10.1002/adfm.202108464.

14. H. Wang, H. Choi, R. Shimogawa, Y. Li, L. Zhang, H. Kim, A. I. Frenkel *Unravelling the origin of reaction-driven aggregation and fragmentation of atomically dispersed Pt catalyst on ceria support* DOI https://doi.org/10.1039/D4NR01396D

15. H. Wang, R. Shimogawa, L. Zhang, L. Ma, S. N. Ehrlich, N. Marinkovic, Y. Li, A. I. Frenkel *Migration and aggregation of Pt atoms on metal oxide-suppored ceria nanodomes control reverse water gas shift reaction activity* Commun. Chem. **6**, 264 (2023)

16. Y. Li, H. Wang, H. Song, N. Rui, M. Kottwitz, S. D. Senanayake, R. G. Nuzzo, Z. Wu, D.-e. Jiang, A. I.Frenkel*Active site of atomically dispersed Pt supported on Gd-doped ceria with improved low temperature performance for CO oxidation* Chem. Science 14, 12582-12588 (2023)

17. H. Wang, N. Rui, S. D. Senanayake, L. Zhang, Y. Li, A. I. Frenkel*Tuning the placement of Pt "single atoms" on a mixed CeO2-TiO2 support*J. Phys. Chem. C 126, 16187-16193 (2022)

18 H. Wang, M. Kottwitz, N. Rui, S. Senanayake, N. Marinkovic, Y. Li, R. G. Nuzzo, A. I. Frenkel *Aliovalent doping of CeO2 improves the stability of atomically dispersed Pt* ACS Appl. Mater. Interf. **13**, 52736-52742 (2021)

19 M. Kottwitz, Y. Li, H. Wang, A. I. Frenkel, R. G. Nuzzo*Single atom catalysts: A review of characterization methods*Chemistry-Methods **1**, 278-294 (2021)

20.Y. Li, A. I. Frenkel. Deciphering *the local environment of single –atom catalysts with X-ray absorption spectroscopy* Acc. Chem. Res. **54**, 2660-2669 (2021)

21. DeRita, L.; Resasco, J.; Dai, S.; Boubnov, A.; Thang, H. V.; Hoffman, A. S.; Ro, I.; Graham, G. W.; Bare, S. R.; Pacchioni, G.; Pan, X.; Christopher, P. Structural Evolution of Atomically Dispersed Pt Catalysts Dictates Reactivity. *Nat. Mater.* **2019**, *18* (7), 746–751. https://doi.org/10.1038/s41563-019-0349-9.

22. Palomino, Robert M., Eli Stavitski, Iradwikanari Waluyo, Yu-chen Karen Chen-Wiegart, Milinda Abeykoon, Jerzy T. Sadowski, Jose A. Rodriguez, Anatoly I. Frenkel, and Sanjaya D. Senanayake. "New in-situ and operando facilities for catalysis science at NSLS-II: The deployment of real-time, chemical, and structure-sensitive X-ray probes." *Synchrotron Radiation News* 30, no. 2 (2017): 30-

23.. Hein, J. R., Koschinsky, A. & Kuhn, T. Deep-ocean polymetallic nodules as a resource for critical materials. *Nature Reviews Earth & Environment* **1**, 158–169 (2020).

24. Shen, Y. F. *et al.* Manganese Oxide Octahedral Molecular Sieves: Preparation, Characterization, and Applications. *Science* **260**, 511–515 (1993).

25. Hao, Y.; Hung, S.-F.; Wang, L.; Deng, L.; Zeng, W.-J.; Zhang, C.; Lin, Z.-Y.; Kuo, C.-H.; Wang, Y.; Zhang, Y.; Chen, H.-Y.; Hu, F.; Li, L.; Peng, S. Designing Neighboring-Site Activation of Single Atom via Tunnel Ions for Boosting Acidic Oxygen Evolution. *Nature Communications* **2024**, *15* (1), 8015. https://doi.org/10.1038/s41467-024-52410-6.

26. Yang, H.; Zhang, X.; Yu, Y.; Chen, Z.; Liu, Q.; Li, Y.; Cheong, W.-C.; Qi, D.; Zhuang, Z.; Peng, Q.; Chen, X.; Xiao, H.; Chen, C.; Li, Y. Manganese Vacancy-Confined Single-Atom Ag in Cryptomelane Nanorods for Efficient Wacker Oxidation of Styrene Derivatives. *Chem. Sci.* **2021**, *12* (17), 6099–6106. https://doi.org/10.1039/D1SC00700A.

27. Hao, X.; Dai, L.; Deng, J.; Liu, Y.; Jing, L.; Wang, J.; Pei, W.; Zhang, X.; Hou, Z.; Dai, H. Nanotubular OMS-2 Supported Single-Atom Platinum Catalysts Highly Active for Benzene Oxidation. *J. Phys. Chem. C* **2021**, *125* (32), 17696–17708. https://doi.org/10.1021/acs.jpcc.1c04579.

28. Zhang, L.; Dai, X.; Li, T.; Liu, C.; Wang, B.; Li, G.; Zhao, P.; Cui, X. Pd Single-Atom Decorated OMS-2 Nanorod for Efficient Silane Oxidation. *New J. Chem.* **2024**, *48* (20), 9333–9339. https://doi.org/10.1039/D4NJ01405G.

29. Resende, K. A.; Teles, C. A.; Jacobs, G.; Davis, B. H.; Cronauer, D. C.; Jeremy Kropf, A.; Marshall, C. L.; Hori, C. E.; Noronha, F. B. Hydrodeoxygenation of Phenol over Zirconia Supported Pd Bimetallic Catalysts. The Effect of Second Metal on Catalyst Performance. *Applied Catalysis B: Environmental* **2018**, *232*, 213–231. https://doi.org/10.1016/j.apcatb.2018.03.041.

30. Riley, C.; Zhou, S.; Kunwar, D.; De La Riva, A.; Peterson, E.; Payne, R.; Gao, L.; Lin, S.; Guo, H.; Datye, A. Design of Effective Catalysts for Selective Alkyne Hydrogenation by Doping of Ceria with a Single-Atom Promotor. *J. Am. Chem. Soc.* **2018**, *140* (40), 12964–12973. https://doi.org/10.1021/jacs.8b07789.

31. Millet, M.-M.; Algara-Siller, G.; Wrabetz, S.; Mazheika, A.; Girgsdies, F.; Teschner, D.; Seitz, F.; Tarasov, A.; Levchenko, S. V.; Schlögl, R.; Frei, E. Ni Single Atom Catalysts for CO2 Activation. *J. Am. Chem. Soc.* **2019**, *141* (6), 2451–2461. https://doi.org/10.1021/jacs.8b11729.

32. Sabaté, Ferran, and María J. Sabater. 2021. "Recent Manganese Oxide Octahedral Molecular Sieves (OMS–2) with Isomorphically Substituted Cationic Dopants and Their Catalytic Applications" *Catalysts* 11, no. 10: 1147. https://doi.org/10.3390/catal11101147

33. Zhou, W. *et al.* Single Atom Microscopy. *Microscopy and Microanalysis* **18**, 1342–1354 (2012).

34. Kattel, S.; Yan, B.; Chen, J. G.; Liu, P. CO2 Hydrogenation on Pt, Pt/SiO2 and Pt/TiO2: Importance of Synergy between Pt and Oxide Support. *Journal of Catalysis* **2016**, *343*, 115–126. https://doi.org/10.1016/j.jcat.2015.12.019.

35. Moncada, J. *et al.* Structural and Chemical Evolution of an Inverse CeOx/Cu Catalyst under CO2 Hydrogenation: Tunning Oxide Morphology to Improve Activity and Selectivity. *ACS Catal.* **13**, 15248–15258 (2023).

36. Wong, A.; Liu, Q.; Griffin, S.; Nicholls, A.; Regalbuto, J. R. Synthesis of Ultrasmall, Homogeneously Alloyed, Bimetallic Nanoparticles on Silica Supports. *Science* **2017**, *358* (6369), 1427–1430. https://doi.org/10.1126/science.aao6538.

37. Yuan, Y.; Wood, S. M.; He, K.; Yao, W.; Tompsett, D.; Lu, J.; Nie, A.; Islam, M. S.; Shahbazian-Yassar, R. Atomistic Insights into the Oriented Attachment of Tunnel-Based Oxide Nanostructures. *ACS Nano* **2016**, *10* (1), 539–548. https://doi.org/10.1021/acsnano.5b05535.

38. Ma, Y., Luo, J. & Suib, S. L. Syntheses of Birnessites Using Alcohols as Reducing Reagents: Effects of Synthesis Parameters on the Formation of Birnessites. *Chem. Mater.* **11**, 1972–1979 (1999).

39. Momma, K.; Izumi, F. VESTA: A Three-Dimensional Visualization System for Electronic and Structural Analysis. *J Appl Cryst* **2008**, *41* (3), 653–658. https://doi.org/10.1107/S0021889808012016.

40. Li, Y.; Frenkel, A. I. Deciphering the Local Environment of Single-Atom Catalysts with X-Ray Absorption Spectroscopy. *Acc. Chem. Res.* **2021**, *54* (11), 2660–2669. https://doi.org/10.1021/acs.accounts.1c00180.

41. Kottwitz, M.; Li, Y.; Wang, H.; Frenkel, A. I.; Nuzzo, R. G. Single Atom Catalysts: A Review of Characterization Methods. *Chemistry Methods* **2021**, *1* (6), 278–294. https://doi.org/10.1002/cmtd.202100020.

42. Jiménez, J. D.; Lustemberg, P. G.; Danielis, M.; Fernández-Villanueva, E.; Hwang, S.; Waluyo, I.; Hunt, A.; Wierzbicki, D.; Zhang, J.; Qi, L.; Trovarelli, A.; Rodriguez, J. A.; Colussi, S.; Ganduglia-Pirovano, M. V.; Senanayake, S. D. From Methane to Methanol: Pd-iC-CeO2 Catalysts Engineered for High Selectivity via Mechanochemical Synthesis. *J. Am. Chem. Soc.* **2024**, *146* (38), 25986–25999. https://doi.org/10.1021/jacs.4c04815.

43. Tesvara, C. *et al.* Unraveling the CO Oxidation Mechanism over Highly Dispersed Pt Single Atom on Anatase TiO2 (101). *ACS Catal.* 7562–7575 (2024) doi:10.1021/acscatal.4c01018

44. Pecoraro, C. M. *et al.* Pt–TiO2 catalysts for glycerol photoreforming: comparison of anatase, brookite and rutile polymorphs. *Chem. Commun.* **60**, 3782–3785 (2024).

45. Priqueler, J. R. L., Butler, I. S. & Rochon, F. D. An Overview of 195Pt Nuclear Magnetic Resonance Spectroscopy. *Applied Spectroscopy Reviews* **41**, 185–226 (2006).

46.Venkatesh, Amrit, Alicia Lund, Lukas Rochlitz, Ribal Jabbour, Christopher P. Gordon, Georges Menzildjian, Jasmine Viger-Gravel, et al. 2020. "The Structure of Molecular and Surface Platinum Sites Determined by DNP-SENS and Fast MAS 195Pt Solid-State NMR Spectroscopy." *Journal of the American Chemical Society* 142 (44): 18936–45. https://doi.org/10.1021/jacs.0c09101.

47. Krivdin, L. B. Computational NMR of heavy nuclei involving 109Ag, 113Cd, 119Sn, 125Te, 195Pt, 199Hg, 205Tl, and 207Pb. *Russian Chemical Reviews* **90**, 1166 (2021).

48. Saveleva, V. A. *et al.* Operando Near Ambient Pressure XPS (NAP-XPS) Study of the Pt Electrochemical Oxidation in H2O and H2O/O2 Ambients. *J. Phys. Chem. C* **120**, 15930–15940 (2016).

49. Xie, Z.; Yan, B.; Kattel, S.; Lee, J. H.; Yao, S.; Wu, Q.; Rui, N.; Gomez, E.; Liu, Z.; Xu, W.; Zhang, L.; Chen, J. G. Dry Reforming of Methane over CeO2-Supported Pt-Co Catalysts with Enhanced Activity. *Applied Catalysis B: Environmental* **2018**, *236*, 280–293. https://doi.org/10.1016/j.apcatb.2018.05.035.

50. Hammond, J. S.; Winograd, N. XPS Spectroscopic Study of Potentiostatic and Galvanostatic Oxidation of Pt Electrodes in H2SO4 and HClO4. Journal of Electroanalytical Chemistry and Interfacial Electrochemistry **1977**, 78 (1), 55–69. https://doi.org/10.1016/S0022-0728(77)80422-1

51. Drawdy, J.E., Hoflund, G.B., Gardner, S.D., Yngvadottir, E. and Schryer, D.R. (1990), Effect of pretreatment on a platinized tin oxide catalyst used for low-temperature Co oxidation. Surf. Interface Anal., 16: 369-374. https://doi.org/10.1002/sia.740160178

52. Foord, J. S., Jackman, R. B. & Allen, G. C. An X-ray photoelectron spectroscopic investigation of the oxidation of manganese. *Philosophical Magazine A* **49**, 657–663 (1984).

53. Derevyannikova, E. A. *et al.* Structural Insight into Strong Pt–CeO2 Interaction: From Single Pt Atoms to PtOx Clusters. *J. Phys. Chem. C* **123**, 1320–1334 (2019).

54. Suib, S. L. Synthesis, characterization and catalysis with microporous ferrierites, octahedral molecular sieves, and layered materials. in *Studies in Surface Science and Catalysis* (eds. Chon, H., Woo, S. I. & Park, S.-E.) vol. 102 47–74 (Elsevier, 1996).

55. Chen, X.; He, G.; Li, Y.; Chen, M.; Qin, X.; Zhang, C.; He, H. Identification of a Facile Pathway for Dioxymethylene Conversion to Formate Catalyzed by Surface Hydroxyl on TiO2-Based Catalyst. *ACS Catal.* **2020**, *10* (17), 9706–9715. https://doi.org/10.1021/acscatal.0c01901.

56. Gamba, O.; Noei, H.; Pavelec, J.; Bliem, R.; Schmid, M.; Diebold, U.; Stierle, A.; Parkinson, G. S. Adsorption of Formic Acid on the Fe3O4(001) Surface. *J. Phys. Chem. C* **2015**, *119* (35), 20459–20465. https://doi.org/10.1021/acs.jpcc.5b05560.

57. So, Rachel T., Neal E. Blair, and Andrew L. Masterson. "Carbonate mineral identification and quantification in sediment matrices using diffuse reflectance infrared Fourier transform spectroscopy." *Environmental chemistry letters* 18, no. 5 (2020): 1725-1730.

58.Yoshida, T., Tsuneaki Yamagata, T. H. Tulip, James A. Ibers, and Sei Otsuka. "Cis dihydride diphosphine complexes of platium (II) and their dehydrogenation to form dimeric platinum (0) complexes. The structure of [Pt (tert-Bu) 2P (CH2) 3P (tert-Bu) 2] 2." *Journal of the American Chemical Society* 100, no. 7 (1978): 2063-2073.

59. Yruela, I., S. I. Allakhverdiev, J. V. Ibarra, and V. V. Klimov. "Bicarbonate binding to the water-oxidizing complex in the photosystem II. A Fourier transform infrared spectroscopy study 1." *FEBS letters* 425, no. 3 (1998): 396-400.

60. Shurvell, H. F. "Spectra-structure correlations in the mid-and far-infrared." *Handbook of vibrational spectroscopy* 3 (2006): 1783-1816.

61. Eads, C. N.; Zhong, J.-Q.; Kim, D.; Akter, N.; Chen, Z.; Norton, A. M.; Lee, V.; Kelber, J. A.; Tsapatsis, M.; Boscoboinik, J. A.; Sadowski, J. T.; Zahl, P.; Tong, X.; Stacchiola, D. J.; Head, A. R.; Tenney, S. A. Multi-Modal Surface Analysis of Porous Films under *Operando* Conditions. *AIP Advances* **2020**, *10* (8), 085109. https://doi.org/10.1063/5.0006220.

62. Ravel, B.; Newville, M. ATHENA, ARTEMIS, HEPHAESTUS: Data Analysis for X-Ray Absorption Spectroscopy Using IFEFFIT. *J Synchrotron Rad* **2005**, *12* (4), 537–541. https://doi.org/10.1107/S0909049505012719.

Acknowledgments

The authors acknowledge the US Department of Energy, Office of Basic Energy Sciences, Division of Chemical, Biological, and Geological Sciences under grant DE-FG02-86ER13622 for partially supporting this research. A.I.F. acknowledges the support of XANES and EXAFS data analysis part of this work by the National Science Foundation under grant 2203858. This research used beamline 7-BM (QAS) of the National Synchrotron Light Source II and the Electron Microscopy and Proximal Probes Facilities of the Center for Functional Nanomaterials; both are U.S. DOE Office of Science User Facilities operated for the DOE Office of Science by Brookhaven National Laboratory under Contract No. DE-SC0012704. Beamline operations were supported in part by the Synchrotron Catalysis Consortium (U.S. DOE, Office of Basic Energy Sciences, Grant No. DE-SC0012335). The authors thank Dr. Steven Ehrlich for help with the beamline measurements at the QAS beamline.

Corresponding authors

Steven L. Suib − Unit 3060, Department of Chemistry, University of Connecticut, Storrs, Connecticut 06269-3060, United States; Institute of Materials Science, University of Connecticut, Storrs, Connecticut 06269, United States; orcid.org/0000-0003-3073-311X; Email: steven.suib@ uconn.edu

Author contribution

S.L.S and P.G. supervised the project, A.H designed the AP-XPS and transmission cell, and IR spectroscopy experiments. A.H and I.P. collected the AP-XPS data, D.Z designed the E-TEM experiments, and D.Z and S.M. collected and analyzed E-TEM data. L.P. and C.L. collected the XRF data, H.T. collected the AC-STEM images, M.L. designed and carried out the methanol reactivity tests. H.K. collected Raman spectra and aided in writing the manuscript. L.M, N.M, R.S, and A.I.F helped design and collect XANES/EXAFS data at the QAS beamline, A.I.F. supervised the analysis and modeling of XANES and EXAFS data, A.F performed sample prep and assisted in data acquisition in XANES, and EXAFS experiments, S.S collected the XRD data and analyzed the XRD data, N.E performed and analyzed the Solid-State Nuclear Magnetic Resonance data, S.B conceived the project and wrote the manuscript. H.K. and S.B. contributed equally.

Conflict of interests

The authors declare no conflict of interests.